Journal of Alloys and Compounds 509 (2011) 6030–6035

Contents lists available at ScienceDirect

Journal of Alloys and Compounds

journal homepage: www.elsevier.com/locate/jallcom

Synthesis and electrochemical properties of porous LiV_3O_8 as cathode materials for lithium-ion batteries

Hua Ma, Zhiqing Yuan, Fangyi Cheng, Jing Liang, Zhanliang Tao*, Jun Chen

Institute of New Energy Material Chemistry and Key Laboratory of Advanced Energy Materials Chemistry (Ministry of Education), Nankai University, Tianjin 300071, PR China

ARTICLE INFO

Article history:
Received 1 December 2010
Received in revised form 24 February 2011
Accepted 25 February 2011
Available online 5 March 2011

Keywords:
Porous LiV_3O_8
Sol–gel method
Cathode material
Lithium ion batteries

ABSTRACT

In this paper, we report on the synthesis of porous LiV_3O_8 by using a tartaric acid-assisted sol–gel process and their enhanced electrochemical properties for reversible lithium storage. The crystal structure, morphology and pore texture of the as-synthesized samples are characterized by means of XRD, SEM, TEM/HRTEM and N_2 adsorption/desorption measurements. The results show that the tartaric acid plays a pore-making function and the calcination temperature is an important influential factor to the pore texture. In particular, the porous LiV_3O_8 calcined at 300 °C (LiV_3O_8-300) exhibits hierarchical porous structure with high surface area of 152.4 $m^2\,g^{-1}$. The electrochemical performance of the as-prepared porous LiV_3O_8 as cathode materials for lithium ion batteries is investigated by galvanostatic charge–discharge cycling and electrochemical impedance spectroscopy. The porous LiV_3O_8-300 displays a maximum discharge capacity of 320 mAh g^{-1} and remains 96.3% of its initial discharge capacity after 50 charge/discharge cycles at the current density of 40 mA g^{-1} due to the enhanced charge transfer kinetics with a low apparent activity energy of 35.2 kJ mol^{-1}, suggesting its promising application as the cathode material of Li-ion batteries.

1. Introduction

Exploring cathode material with larger discharge capacity and higher energy density is still the main challenge for developing lithium ion batteries because their electrochemical performance is usually cathode limited [1,2]. Vanadium oxide-based materials have attracted significant attention due to their low-cost, high discharge capacity and high specific energy [3–7]. Among them, the layered lithium trivanadate (LiV_3O_8) can insert reversibly over three Li per formula unit at the tetrahedral sites, making it one of the promising substitutes for expensive $LiCoO_2$ cathode used commercially in lithium ion batteries [8–10]. However, the LiV_3O_8 synthesized by traditional solid-state method suffers from serious capacity loss caused by poor kinetic diffusion of Li^+ ions into LiV_3O_8 tetrahedral sites [11]. To overcome this obstacle, many research efforts have been focused on improving the electrochemical properties of LiV_3O_8 by either developing new synthetic method [12–15] or structural/morphological modification [16–18].

It is found that the grain morphology and crystal shape play a major role on the initial capacity and cyclability of LiV_3O_8 [19,20]. Reducing the particle size and increasing the surface area would improve Li^+ ion diffusion kinetic, leading to higher specific capacities and better cyclability. For example, Xu et al. have showed that LiV_3O_8 nanorods exhibit the highest discharge capacity of 302 mAh g^{-1} and remain 278 mAh g^{-1} after 30 cysles [21]. Liu et al. have demonstrated that single-crystalline LiV_3O_8 nanorods show an initial discharge capacity as high as 348 mAh g^{-1} at 20 mA g^{-1}, and still remain at 303 mAh g^{-1} at 50 mA g^{-1} [22]. Li et al. have reported that carnation-like LiV_3O_8 nanostrutures present the highest capacity of 357 mAh g^{-1} and enhanced cycling performance [23]. Recently, Liang and co-workers have demonstrated that the LiV_3O_8 nanorods prepared by a thermal co-decomposition method deliver specific discharge capacities of 320 mAh g^{-1} and 239 mAh g^{-1} at current densities of 100 mA g^{-1} and 1 A g^{-1}, respectively, and exhibit good capacity retention [24]. On the other hand, it should be noted that converting the materials from solid bulk to porous forms, which can decrease the polarization and alleviate the structure stress during the charge/discharge cycling, is an efficient method to improve the electrochemical performance of cathode materials [25,26]. Indeed, Cui et al. have reported that the LiV_3O_8 nanotubes with inner diameter of 30–50 nm have a high initial discharge capacity of 457 mhA g^{-1} at current density of 30 mA g^{-1}, but the discharge capacity decreases quickly [27]. To the best of our knowledge, the controllable synthesis and electrochemical properties of LiV_3O_8 with mesoporous structure has not been reported yet. Herein, we present a facile and controllable route to synthesize porous LiV_3O_8 by a tartaric acid-assisted sol–gel method. Furthermore, the specific capacity, cycling performance

* Corresponding author. Fax: +86 22 23506808.
E-mail address: taozhl@nankai.edu.cn (Z. Tao).

0925-8388/$ – see front matter © 2011 Elsevier B.V. All rights reserved.
doi:10.1016/j.jallcom.2011.02.161

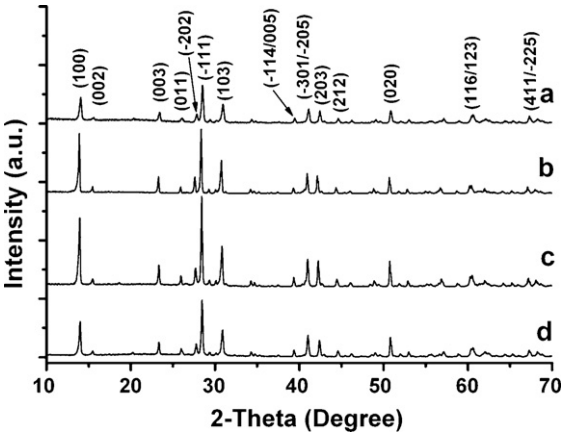

Fig. 1. XRD patterns of the as-prepared LiV_3O_8 samples: (a) LiV_3O_8-300, (b) LiV_3O_8-400, (c) LiV_3O_8-500 and (d) LiV_3O_8-300 bulk.

and electrochemical kinetics of the as-synthesized porous LiV_3O_8 were investigated in detail, indicating their potential application as the cathode material for rechargeable Li-ion batteries.

2. Experimental details

2.1. Synthesis and characterization of porous LiV_3O_8

The porous LiV_3O_8 were synthesized through a sol–gel route. All of the chemical reagents were of analytical grade and used without further purification. In a typical preparation of porous LiV_3O_8, 0.001 mol of $LiOH{\cdot}H_2O$, 0.003 mol of NH_4VO_3 and 0.003 mol of tartaric acid ($C_8H_{14}O_6$) were dissolved into 20 mL of deionized water under magnetic stirred. Then, the resultant solution was dried in air at 80 °C until a black xerogel was obtained. Afterwards, the xerogel was calcined at 300, 400 and 500 °C in a muffle furnace oven for 2 h to obtain the samples, which were denoted as LiV_3O_8-300, LiV_3O_8-400 and LiV_3O_8-500, respectively. For comparison, the LiV_3O_8 bulk particles calcined at 300 °C (LiV_3O_8-300 bulk) were prepared from the process mentioned above without addition of tartaric acid.

The phase of the as-prepared samples was investigated by powder X-ray diffraction (XRD, Rigaku D/max-2500 X-ray generator, Cu Kα radiation). The morphology and microstructure of the samples were analyzed with scanning electron microscopy (SEM, JEOL JSM-6700F Field Emission, 10 kV), transmission electron microscopy (TEM), and high-resolution TEM (Philips Tecnai T20ST, 200 kV) [28]. The specific surface areas and pore distribution of the products were detected by nitrogen adsorption–desorption measurements (BEL-SORP-mini, BEL, Japan).

2.2. Electrochemical measurements

Electrochemical properties of the as-synthesized samples were studied using two-electrode test cells. The working electrode as cathode was fabricated by compressing a mixture of 85 wt% active material (as-prepared LiV_3O_8 samples), 10 wt% carbon black (Cabot, Vulcan XC-72) and 5 wt% polyvinylidene fluoride (PVDF) onto a Al foil and then drying in vacuum at 80 °C for 24 h. The test cells were assembled in a glove-box (Mikrouna Co., Ltd., Universal 2240/750) filled with pure argon (99.999%), lithium foil as anode and Celgard 2320 as separator. The electrolyte solution was 1.0 mol L^{-1} $LiPF_6$ dissolved in a mixture of ethylene carbonate (EC) and diethyl carbonate (DEC) solution with the volumetric ratio of 1:1.

The capacity and cycling performance of the electrode were investigated by a galvanostatic charge–discharge method using Land battery measurement system (CT2001A, WuHan, PR China) in the potential range of 1.5–3.5 V (vs. Li^+/Li) at current density of 40 mA g^{-1}. The capacity was based on the amount of the active material, excluding the weight of the additives in the electrode. The electrochemical impedance spectroscopy (EIS) was investigated by the Parstat 2273 potentiostat/galvanostat analyzer (AMTECT Company) with an AC voltage of 10 mV amplitude in the frequency range from 1×10^5 to 1×10^{-2} Hz. Prior to EIS measurement, the as-assembled cells were discharged to the requested voltage and held for 4 h to reach the equilibrium state at 20, 30, 40 and 50 °C, respectively. The EIS data were analyzed using ZsimpWin software.

3. Results and discussion

3.1. Structural and morphological Characterization

Fig. 1 shows the XRD patterns of the as-synthesized LiV_3O_8 samples calcined at 300 (LiV_3O_8-300, Fig. 1a), 400 (LiV_3O_8-400, Fig. 1b) and 500 °C (LiV_3O_8-500, Fig. 1c) with and without tartaric acid (LiV_3O_8-300 bulk, Fig. 1d), respectively. It can be seen that the positions of the characteristic peaks of the samples are accordant with each other. All of the characteristic peaks can be indexed into monoclinic LiV_3O_8 with space group of $P21/m$ (JCPDS card no. 72-1193). No peak from other phase has been detected, revealing the high phase purity of the as-synthesized samples. In addition, with increasing the calcination temperature, the intensity of the diffraction peaks becomes stronger, indicating the higher crystallinity.

The influence of tartaric acid and calcination temperature on the morphology of the products was investigated by SEM images, as shown in Fig. 2. The sample synthesized by the sol–gel method, in which the calcination temperature is 300 °C and no tartaric acid was added in the reaction system, is always composed of compact and irregular microparticles with size of about 1–3 μm (Fig. 2a and b). When the tartaric acid is added in the reaction system, the LiV_3O_8 calcined at 300 °C (LiV_3O_8-300) is composed of porous particles with size of about several micrometers, as shown in the overview SEM image (Fig. 2c). Increasing the magnification, it can be seen from Fig. 2d that the LiV_3O_8 microparticles are honeycomb-like in shape with pore size distribution from around 10 nm to several tens of nanometers over the whole area of the LiV_3O_8 particles. This result reveals that the tartaric acid decomposes and releases CO_2 and H_2O gases during the calcination process, which is the key factor in the formation of pores and tunnels in the LiV_3O_8 sample. In addition, it is found that the calcination temperature plays an important role in controlling the pore texture of the LiV_3O_8 samples. The sample calcined at 400 °C (LiV_3O_8-400) is also composed of porous microparticles (Fig. 2e). However, the pore size is in the range of 0.5–1 μm, which is much larger than that of the LiV_3O_8-300. Moreover, the pore wall of LiV_3O_8-400 splits and in fact is assembled by a large number of nanoparticles with size of about 200 nm, as shown in the magnified SEM image (Fig. 2f). When the calcination temperature grows to 500 °C (Fig. 2g and h), the sample (LiV_3O_8-500) consists of a large number of particles with size between 300 and 600 nm, and no obvious porous structure is detected. It is believed that the gas generation rate is varied at different temperature. The increase of the calcination temperature from 300 to 500 °C accelerated the gas generation rate, which results in enlarging the pore size and even destroying the porous structure. Moreover, the change in particle size with temperature can be explained by variation of the growth rate at different temperature. The increase of the calcination temperature from 300 to 500 °C accelerated the growth rate of the particles, which leads the larger size of the products. Thus, the LiV_3O_8-400 and LiV_3O_8-500 samples showed large particles.

Furthermore, TEM technique has been employed to investigate the detailed structure of the as-prepared porous LiV_3O_8-300, as shown in Fig. 3. A low magnification TEM image in Fig. 3a presents the porous structure of the LiV_3O_8-300, which is consistent with the observation in the SEM images (Fig. 2c and d). It can be seen from Fig. 3b that the porous LiV_3O_8 is assembled by aggregate primary nanoparticles with sizes of several tens of nanometers, showing wormhole-like meso- and macroporous structure. In addition, the magnified TEM image in Fig. 3c indicates that the primary nanoparticles present mesoporous structure with pore size between 2 and 4 nm. The high-resolution TEM (Fig. 3d) image taken from the edge of the porous LiV_3O_8 particles shows that the apparent lattice spacing is 0.314 nm, which is in accordance with the interplanar distance of the (−1 1 1) crystal plane of LiV_3O_8. This result is further confirmed in the corresponding fast Fourier transform (FFT) pattern (inset in Fig. 3d), indicating the well-crystallized monoclinic phase of the porous LiV_3O_8-300 sample.

Fig. 4 shows the N_2 adsorption/desorption isotherms and corresponding Barrett–Joyner–Halenda (BJH) pore size distribution

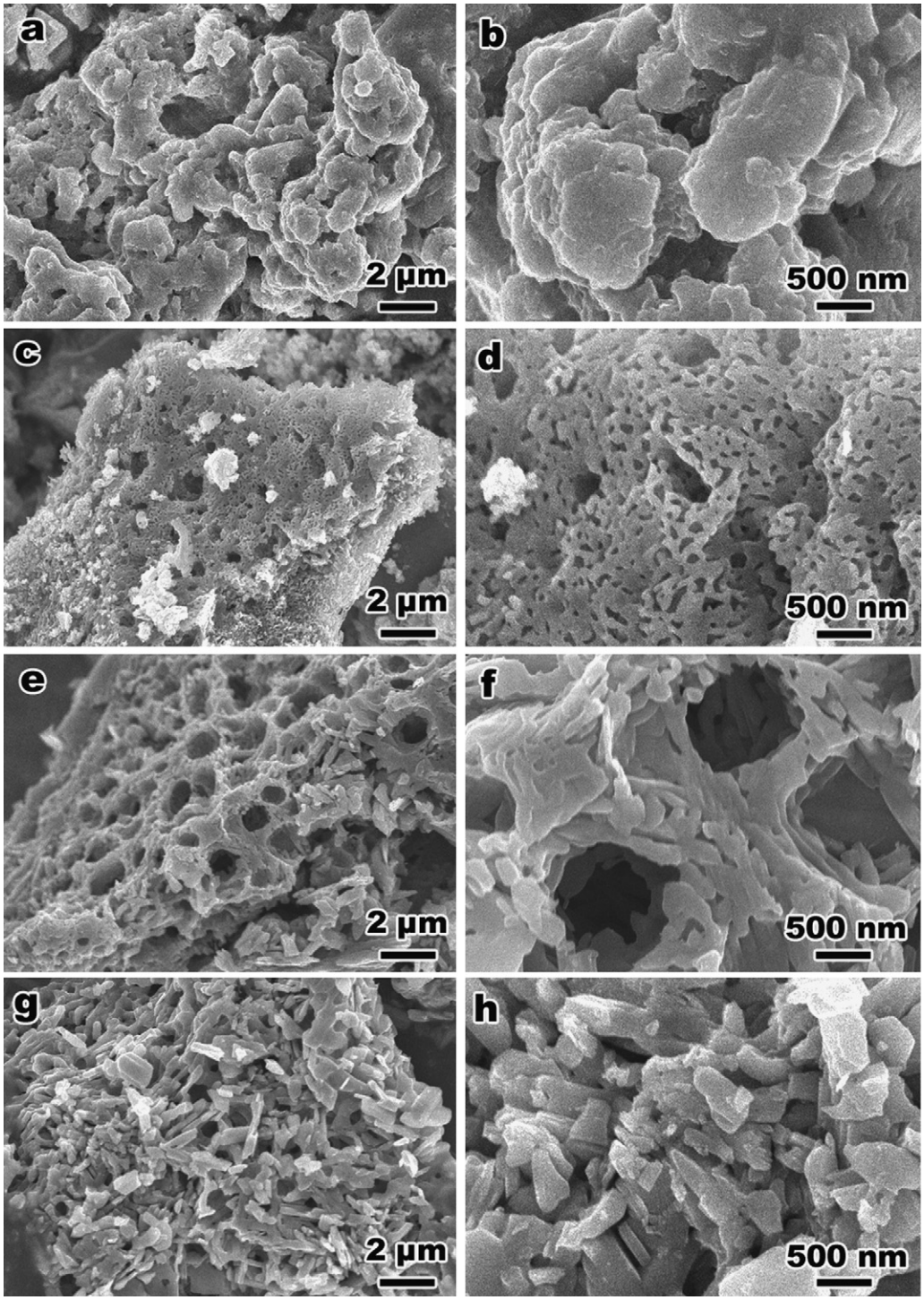

Fig. 2. SEM images of the as-synthesized LiV_3O_8 samples: (a, b) LiV_3O_8-300 bulk, (c, d) LiV_3O_8-300, (e, f) LiV_3O_8-400 and (g, h) LiV_3O_8-500.

of the porous LiV_3O_8-300 sample. The shape of the isotherms indicates that the as-synthesized LiV_3O_8-300 contains multimodal pores (Fig. 4a) [29]. The steep increase of N_2 adsorbed volume at high relative pressure reveals the presence of macropores in the sample, while, the H3 type hysteresis loop in the isotherms confirms the mesoporosity. The BJH calculation (Fig. 4b) reveals that the LiV_3O_8-300 sample presents a narrow pore size distribution between 2 and 4 nm, suggesting the ordered pore structure. Besides the main pore size distribution, in fact, the BJH calculation reveals that the LiV_3O_8-300 sample presents pore size in the range of 10–15 and 20–30 nm from the magnified BJH curve marked by rectangle frame (Inset in Fig. 4b), which is in agreement with the SEM images. Furthermore, the total specific surface area of LiV_3O_8-300 estimated from the Brunauer–Emmett–Teller (BET) method is 152.4 $m^2 g^{-1}$, which is much higher than that of the as-synthesized LiV_3O_8-300 bulk (7.8 $m^2 g^{-1}$). As far as we know, it is the highest surface area for LiV_3O_8 that have ever been reported to date [20,22]. This result suggests that the tartaric acid-assisted sol–gel process is an effective way for obtaining hierarchical porous structure with enlarged specific surface areas, which can provide more active sites for lithium storage.

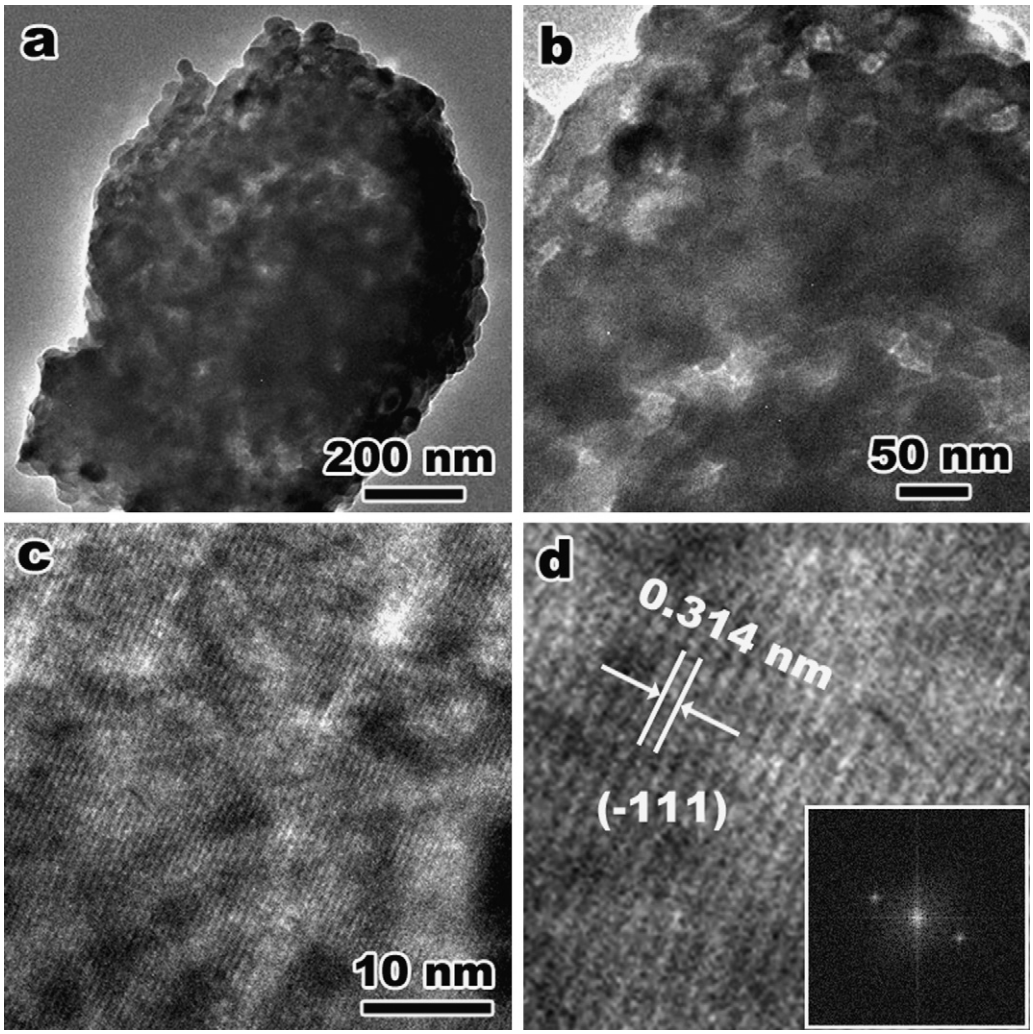

Fig. 3. (a–c) TEM and (d) HRTEM images of the as-prepared LiV_3O_8-300. Inset in (d) shows the corresponding FFT pattern.

3.2. Electrochemical Characterization

Fig. 5 shows the discharge–charge curves and cyclability of the as-synthesized LiV_3O_8 samples at current density of 40 mA g^{-1}. As shown in Fig. 5a, the voltage profiles of the as-synthesized LiV_3O_8-300, LiV_3O_8-400, LiV_3O_8-500 and LiV_3O_8-300 bulk electrodes present a similar shape. The potential decreases with the discharge processing, showing two voltage plateaus at about 2.8 and 2.5 V (vs. Li^+/Li), respectively. It has been reported that the discharge plateau of 2.8 V is ascribed to single-phase lithium insertion process for LiV_3O_8, and the 2.5 V plateau reveals the two-phase transformation between $Li_{1+x}V_3O_8$ ($1 \leq x \leq 2$) and $Li_4V_3O_8$ [22,30]. Meanwhile, the charge profile shows one flat voltage plateau at around 2.72 V, indicating occurrence of lithium extraction from the $Li_4V_3O_8$ phase and simultaneous formation of the LiV_3O_8 phase. In fact, one obscure plateau at around 2.85 V also can be observed in the charge profile, which is an electrochemical signature of a delithiation process in the single LiV_3O_8 phase [11]. Furthermore, the LiV_3O_8-300 exhibits longer potential plateau, delivering much higher discharge capacity than these of other samples. The increase in the discharge capacity is attributed to the fact that the micro- and mesopores in the LiV_3O_8-300 can provide more active sites for lithium ion accommodation.

The cyclic performance of the samples at 40 mA g^{-1} in the potential range of 1.5–3.5 V (vs. Li^+/Li) was investigated. As shown in Fig. 5b, the LiV_3O_8-300 bulk obtained without addition of tartaric acid presents an initial discharge capacity of 258 mAh g^{-1} but with a serious capacity fading in the cycling. The discharge capacity decreases quickly to 139 mAh g^{-1} after 50 cycles, corresponding to only 53.9% of the initial value. The capacity decay for LiV_3O_8 obtained with addition of tartaric acid is far slower compared to the LiV_3O_8-300 bulk. In particular, the porous LiV_3O_8-300 shows a high initial discharge capacity of 301 mAh g^{-1} and the discharge capacity increases to a maximum value of 320 mAh g^{-1} at the 3rd cycle following with a slight decrease upon cycling. This result can be explained by an activation process. After a few cycles, more lithium ions can be accommodated in the porous LiV_3O_8-300 through the hierarchical pores and inner tunnel. Thus, an increase in capacity was observed. After 50 charge/discharge cycles, the porous LiV_3O_8-300 still maintains a capacity of 290 mAh g^{-1}, corresponding to 96.3% of its initial discharge capacity. It is noted that the porous LiV_3O_8-300 outperforms the previously reported LiV_3O_8 rods and polypyrrole-LiV_3O_8 composite in discharge capacity [15,17], and the capacity retention of the porous LiV_3O_8-300 is comparable to the nanostructured LiV_3O_8 [16,22]. Although the LiV_3O_8-400 and LiV_3O_8-500 show lower initial discharge capacities (255 and 202 mAh g^{-1}, respectively) than that of the LiV_3O_8-300 bulk, they exhibit better cycling stability. At 50th charge/discharge cycle, the discharge capacities of the LiV_3O_8-400 and LiV_3O_8-500 keep at 202 and 166 mAh g^{-1}, respectively. Thus, the surface morphology has a strong influence on the capacity and cycling performance of LiV_3O_8 electrode.

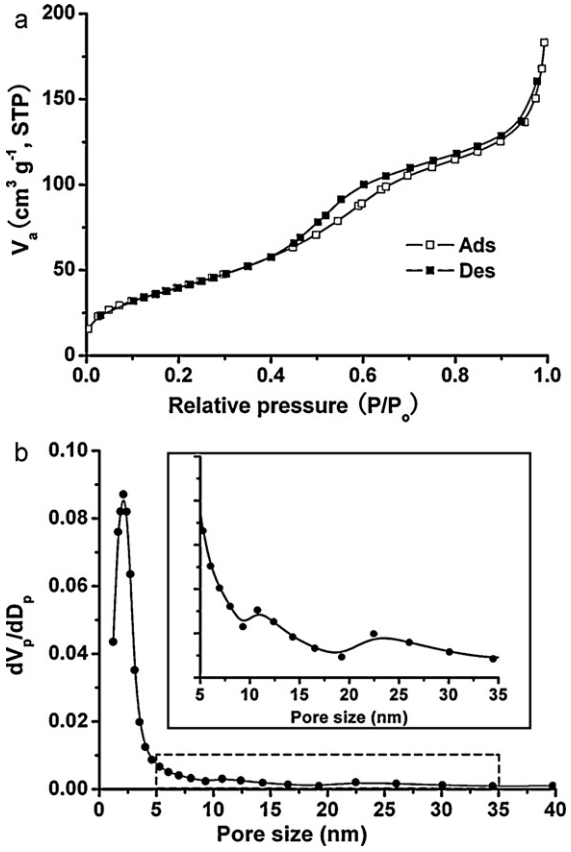

Fig. 4. (a) N_2 adsorption–desorption isotherms and (b) BJH pore size distribution curve of the as-synthesized LiV_3O_8-300. Inset in (b) shows the magnified region of BJH curve marked by rectangle frame in (b).

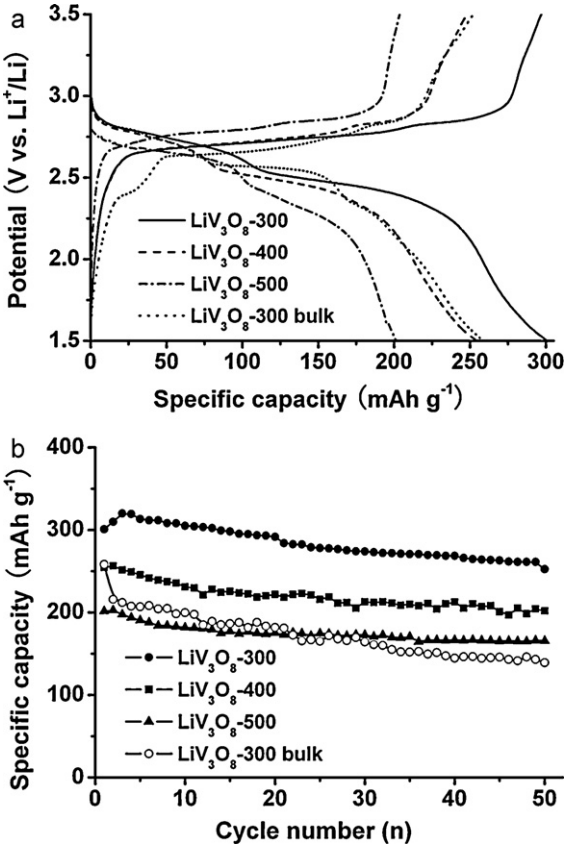

Fig. 5. (a) The first galvanostatic charge–discharge curves and (b) the cycling performance of the as-prepared LiV_3O_8-300, LiV_3O_8-400, LiV_3O_8-500 and LiV_3O_8-300 bulk electrodes in the potential range of 1.5–3.5 V (vs. Li^+/Li) at the current density of 40 mA g^{-1}.

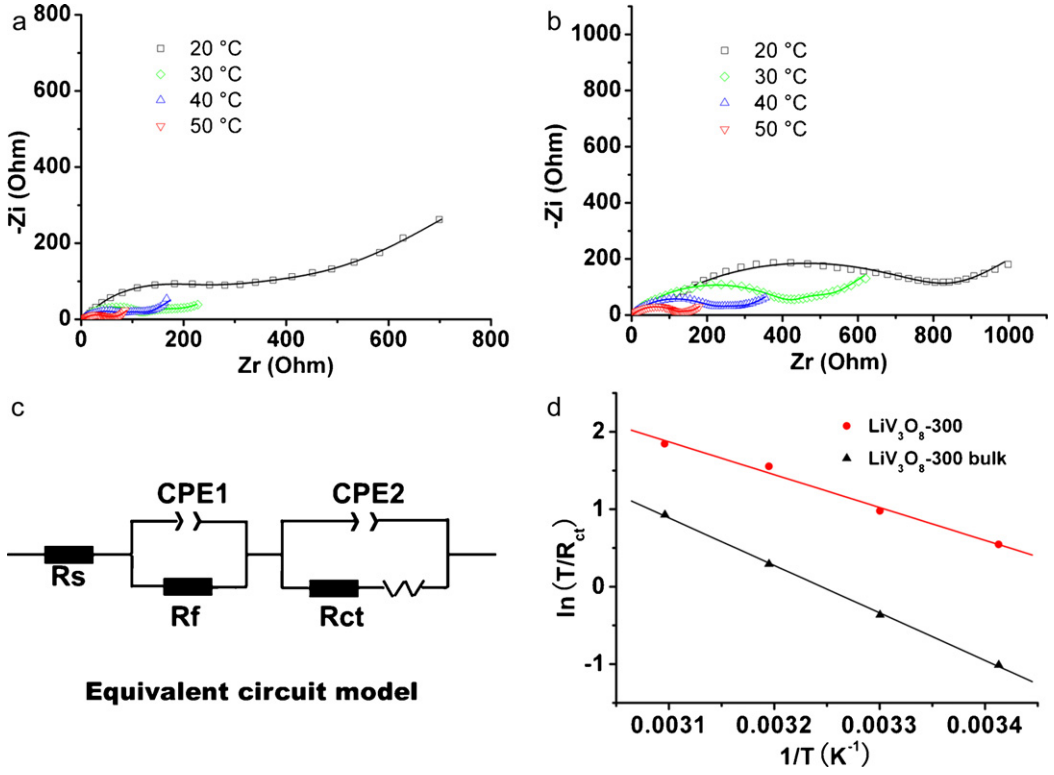

Fig. 6. Electrochemical impedance spectroscopy (EIS) for the (a) LiV_3O_8-300 and (b) LiV_3O_8-300 bulk electrodes at 2.5 V (vs. Li^+/Li) on their 5th discharge at temperature of 20, 30, 40 and 50 °C. The solid lines in (a) and (b) give the simulated lines. (c) The equivalent circuit for the electrochemical impedance spectrum and (d) Arrhenius plots of $\ln(T/R_{ct})$ vs. $1/T$ for the LiV_3O_8-300 and LiV_3O_8-300 bulk electrodes.

Furthermore, the electrochemical impedance spectroscopy (EIS) was used to study the lithium ion intercalation kinetics. Panels a and b in Fig. 6 shows the EIS measured at different temperature for the porous LiV_3O_8-300 and LiV_3O_8-300 bulk electrodes at 2.5 V (vs. Li^+/Li) on their 5th discharge cycle. It can be found that the impedance curves show two partially overlapped semicircles in the high- and medium-frequency region and an inclined line in the low-frequency region. In the light of the equivalent circuit shown in Fig. 6c, the semicircle could be assigned to the combination of the electrode/electrolyte interface film resistance (R_f) and charge transfer resistance (R_{ct}), while the linear portion could be considered as Warburg impedance [31]. The values of R_{ct} for porous LiV_3O_8-300 are 170.0, 113.8, 66.2 and 51.1 Ω at 20, 30, 40 and 50 °C, respectively, which are smaller than those of LiV_3O_8-300 bulk (806.0, 436.4, 233.9 and 127.6 Ω) at the corresponding temperatures, indicating that the porous structure facilitate the lithium ions transfer and intercalation. The apparent activation energies (E_a) for lithium intercalation were estimated by electrochemical impedance spectroscopy (EIS) [6]. The apparent activation energies ($E_a = -Rk$, R is the gas constant and k is the slope of the straight line in Fig. 6d) of porous LiV_3O_8-300 and LiV_3O_8-300 bulk are calculated to be 35.2 and 50.9 kJ mol^{-1}, respectively. The lower activation energy of porous LiV_3O_8-300 indicates the enhanced kinetics of lithium ion diffusion.

On the basis of the results mentioned above, the porous LiV_3O_8 exhibit enhanced electrochemical performance. The reasonable explanation is discussed as follows. First, the porous structure provides high surface area and extra tunnel to make the efficient contact of the porous LiV_3O_8 with the electrolyte, which decreases the polarization of the electrode. Second, the continuous and thin pore walls also facilitate the transport of electron and lithium ion. Thus, the charge transfer kinetics is improved. Finally, the porous framework could act as a buffer to alleviate the LiV_3O_8 volume change during charging/discharging, resulting in the improved cycling stability. Consequently, the porous LiV_3O_8-300 presents enhanced discharge capacity and cycling performance

4. Conclusions

The pore size and surface texture of porous LiV_3O_8, which were prepared by a tartaric acid assisted sol–gel method, were readily controlled by altering the calcination temperature. The as-prepared porous LiV_3O_8-300 with surface area of 152.4 m^2 g^{-1} exhibited a maximum discharge capacity of 320 mAh g^{-1} at current density of 40 mA g^{-1} and remained 96.3% of its initial discharge capacity after 50 cycles. The improved electrochemical properties of the porous LiV_3O_8-300 is contributed to their enhanced charge transfer kinetics, indicating their potential application as cathode material in lithium ion batteries.

Acknowledgments

This study was supported by the Research Programs of National NSFC (21076108), 973 (2011CB935904), Tianjin City (10JCYBJC08400 and 10SYSYJC27600) and Postdoctoral Science Foundation (20100470797) from PR China.

References

[1] J.B. Goodenough, Y. Kim, Chem. Mater. 22 (2010) 587–603.
[2] J. Chen, F.Y. Cheng, Acc. Chem. Res. 42 (2009) 713–723.
[3] S.M. Lee, H.S. Kim, T.Y. Seong, J. Alloys Compd. 509 (2011) 3136–3140.
[4] S.Y. Zhan, Y.J. Wei, X.F. Bie, C.Z. Wang, F. Du, G. Chen, F. Hu, J. Alloys Compd. 502 (2010) 92–96.
[5] A. Bouzidi, N. Benramdane, M. Medles, M. Khadraoui, S. Bresson, C. Mathieu, R. Desfeux, M. E.I. Marssi, J. Alloys Compd. 503 (2010) 445–448.
[6] H. Ma, S.Y. Zhang, W.Q. Ji, Z.L. Tao, J. Chen, J. Am. Chem. Soc. 130 (2008) 5361–5367.
[7] S.L. Chou, J.Z. Wang, J.Z. Sun, D. Wexler, M. Forsyth, H.K. Liu, D.R. MacFarlane, S.X. Dou, Chem. Mater. 20 (2008) 7044–7051.
[8] K. West, B. Zachau-Christiansen, S. Skaarup, Y. Saidi, J. Barker, I.I. Olsen, R. Pynenburg, R. Koksbang, J. Electrochem. Soc. 143 (1996) 820–825.
[9] Y.C. Si, L.F. Jiao, H.T. Yuan, H.X. Li, Y.M. Wang, J. Alloys Compd. 486 (2009) 400–405.
[10] L. Liu, L.F. Jiao, J.L. Sun, Y.H. Zhang, M. Zhao, H.T. Yuan, Y.M. Wang, J. Alloys Compd. 471 (2009) 352–356.
[11] J. Kawakite, T. Miura, T. Kishi, J. Power Sources 83 (1999) 79–83.
[12] H.M. Liu, Y.G. Wang, W.S. Yang, H.S. Zhou, Electrochim. Acta 56 (2011) 1392–1398.
[13] J.J. Feng, X.Z. Liu, X.M. Zhang, J.Z. Jiang, J. Zhao, M. Wang, J. Electrochem. Soc. 156 (2009) A768–A771.
[14] Q. Shi, R.Z. Hu, L.Z. Ouyang, M.Q. Zeng, M. Zhu, Electrochem. Commun. 11 (2009) 2169–2172.
[15] A. Sakunthala, M.V. Reddy, S. Selvasekarapandian, B.V.R. Chowdari, P.C. Selvin, J. Phys. Chem. C 114 (2010) 8099–8107.
[16] Y.X. Gu, D.R. Chen, X.L. Jiao, F.F. Liu, J. Mater. Chem. 16 (2006) 4361–4366.
[17] C.Q. Feng, S.Y. Chew, Z.P. Guo, J.Z. Wang, H.K. Liu, J. Power Sources 174 (2007) 1095–1099.
[18] Y.M. Liu, X.C. Zhou, Y.L. Guo, Electrochim. Acta 54 (2009) 3184–3190.
[19] S. Jouanneau, A. Verbaere, S. Lascaud, D. Guyomard, Solid State Ionics 177 (2006) 311–315.
[20] J.Q. Xu, H.L. Zhang, T. Zhang, Q.Y. Pan, Y.H. Cui, J. Alloys Compd. 467 (2009) 327–331.
[21] H.Y. Xu, H. Wang, Z.Q. Song, Y.W. Wang, H. Yan, M. Yoshimura, Electrochim. Acta 49 (2004) 349–353.
[22] H.M. Liu, Y.G. Wang, K.X. Wang, Y.R. Wang, H.S. Zhou, J. Power Sources 192 (2009) 668–673.
[23] X.L. Li, P.P. Li, M. Luo, X.Y. Chen, J.J. Chen, J. Solid State Electrochem. 14 (2010) 1325–1332.
[24] A.Q. Pan, J. Liu, J.G. Zhang, G.Z. Cao, W. Xu, Z.M. Nie, X. Jie, D.W. Choi, B.W. Arey, C.M. Wang, S.Q. Liang, J. Mater. Chem. 21 (2011) 1153–1161.
[25] F.Y. Cheng, Z.L. Tao, J. Liang, J. Chen, Chem. Mater. 20 (2008) 667–681.
[26] C.Q. Feng, S.Y. Wang, R. Zeng, Z.P. Guo, K. Konstantinov, H.K. Liu, J. Power Sources 184 (2008) 485–488.
[27] C.J. Cui, G.M. Wu, J. Shen, B. Zhou, Z.H. Zhang, H.Y. Yang, S.F. She, Electrochim. Acta 55 (2010) 2536–2541.
[28] H. Ma, W.Q. Ji, J.Z. Zhao, J. Liang, J. Chen, J. Alloys Compd. 474 (2009) 584–589.
[29] M. Kruk, M. Jaroniec, Chem. Mater. 13 (2001) 3169–3183.
[30] S. Jouanneau, A. Le Gal La Salle, A. Verbaere, D. Guyomard, J. Electrochem. Soc. 152 (2005) A1660–A1667.
[31] C.H. Chen, J. Liu, K. Amine, J. Power Sources 96 (2001) 321–328.